

<https://doi.org/10.1038/s41524-025-01563-z>

Active learning of effective Hamiltonian for super-large-scale atomic structures

Check for updates

Xingyue Ma ^{1,2}, Hongying Chen ^{1,2}, Ri He ³, Zhanbo Yu ^{1,2}, Sergei Prokhorenko ⁴, Zheng Wen ⁵, Zhicheng Zhong ^{6,7}, Jorge Íñiguez-González ^{8,9}, L. Bellaiche ⁴, Di Wu ^{1,2} & Yurong Yang ^{1,2}

The first-principles-based effective Hamiltonian scheme provides one of the most accurate modeling techniques for large-scale structures, especially for ferroelectrics. However, the parameterization of the effective Hamiltonian is complicated and can be difficult for some complex systems such as high-entropy perovskites. Here, we propose a general form of effective Hamiltonian and develop an active machine-learning approach to parameterize the effective Hamiltonian based on Bayesian linear regression. The parameterization is employed in molecular dynamics simulations with the prediction of energy, forces, stress and their uncertainties at each step, which decides whether first-principles calculations are executed to retrain the parameters. Structures of BaTiO_3 , PbTiO_3 , $\text{Pb}(\text{Zr}_{0.75}\text{Ti}_{0.25})\text{O}_3$, and $(\text{Pb},\text{Sr})\text{TiO}_3$ system are taken as examples to show the accuracy of this approach, as compared with conventional parametrization method and experiments. This machine-learning approach provides a universal and automatic way to compute the effective Hamiltonian parameters for any considered complex systems with super-large-scale (more than 10^7 atoms) atomic structures.

First-principles (FP) methods based on density functional theory (DFT) have become indispensable to scientific research in physics, chemistry, materials, and other fields¹. However, studying the structure and properties of large-scale structures, such as thermally-driven phase transitions or multidomain states in ferroic materials, remains a great challenge due to the large computational cost of using ab initio molecular dynamics. The recent development of first-principles-based machine-learning force fields (MLFFs) for molecular dynamics makes it possible to study the large-scale structure with good accuracy, similar to first-principles^{2–6}. Another method that can handle large-scale structures is the first-principles-based effective Hamiltonian, which is also physically interpretable and faster than MLFF-based molecular dynamics. The first-principles-based effective Hamiltonian approach has been proposed to describe the couplings between local order parameters (both long-ranged and short-ranged), in which the coupling parameters for the effective Hamiltonian are computed by first principles and have direct physical meanings^{7,8}. Such a method has successfully reproduced or predicted the structure phase transitions^{9–12} and various properties of many compounds^{11,13–16}, such as piezoelectric effect,

electrocaloric effect, dielectric response and optical response, and so on. Moreover, interesting complex polar vortices¹⁷, ferroelectric labyrinthine domains¹⁸, polar skyrmion¹⁹, and merons²⁰ were also recently found by effective Hamiltonian methods in complex perovskite systems.

For the effective Hamiltonian, the parameters of order-parameter-couplings are obtained by fitting FP calculations for many structures with special structural distortions^{7,21}. These fitting procedures may be tricky and complex, and some approximations (such as virtual crystal approximation)^{22–24} may need to be included, leading to uncertainties and even errors for some complex interactions and structures. Additional manual adjustment of the values of some parameters may be necessary to reproduce experimental results^{11,12}. Therefore, to avoid complications and some approximations in the parameterization of the effective Hamiltonian, a new scheme of parameterization in a reliable, precise, convenient, and automatic way is highly demanded. Recently, there have been some reports of building and fitting first-principle-based models using machine learning and energy mapping schemes^{25–27}. Though mainly focused on *magnetic* effective Hamiltonian, they also shed some light on the building and

¹National Laboratory of Solid State Microstructures and Collaborative Innovation Center of Advanced Microstructures, Nanjing University, Nanjing, China. ²Jiangsu Key Laboratory of Artificial Functional Materials, Department of Materials Science and Engineering, Nanjing University, Nanjing, China. ³Key Laboratory of Magnetic Materials Devices & Zhejiang Province Key Laboratory of Magnetic Materials and Application Technology, Ningbo Institute of Materials Technology and Engineering, Chinese Academy of Sciences, Ningbo, China. ⁴Smart Functional Materials Center, Physics Department and Institute for Nanoscience and Engineering, University of Arkansas, Fayetteville, AR, USA. ⁵College of Electronics and Information, Qingdao University, Qingdao, China. ⁶Department of Physics, University of Science and Technology of China, Hefei, China. ⁷Suzhou Institute for Advanced Research, University of Science and Technology of China, Suzhou, China. ⁸Smart Materials Unit, Luxembourg Institute of Science and Technology (LIST), Avenue des Hauts-Fourneaux 5, Esch/Alzette, Luxembourg. ⁹Department of Physics and Materials Science, University of Luxembourg, 41 Rue du Brill, Belvaux, Luxembourg. e-mail: diwu@nju.edu.cn; yangr@nju.edu.cn

parameterization of the *atomic* effective Hamiltonian with machine-learning-based approaches.

In this article, a general effective Hamiltonian is proposed, and an on-the-fly active-learning method is applied to the parameterization of this general effective Hamiltonian. Only a small number of FP calculations are required in this parameterization process. Perovskite structures [BaTiO₃, PbTiO₃, Pb(Zr,Ti)O₃, and (Pb,Sr)TiO₃] are taken as examples, where the active-learning method provides simulations results that agree very well with other first-principles-based calculations and experiments. Such a reliable and highly-automatic way to construct the effective Hamiltonian parameters makes it possible to mimic the super-large scale and complex atomic structures.

Results

Effective Hamiltonian

The effective Hamiltonian describes the couplings between order parameters, and it is developed based on the Taylor expansion of small distortions around the reference structure. Various order parameters are considered (see Fig. 1a for an example), which is further explained in “Mode and basis”. Briefly, the degrees of freedom of the effective Hamiltonian are: (1) local modes attributed to each unit cell i , to be denoted as $\{s_1\}, \{s_2\}, \dots$, representing atomic displacements with respect to the reference structure, usually associated with different phonon modes; (2) the homogeneous strain tensor η ; and (3) the variable $\{\sigma\}$ representing the atom occupation in unit cell i [for example, in Pb(Zr,Ti)O₃, $\sigma_i = 1$ (respectively, $\sigma_i = 2$) represents a Ti (respectively, Zr) atom sitting in unit cell i ²²].

The potential energy E_{pot} contains four main parts: (i) E_{single} , which contains the self energies of each mode, involving only one site in each term; (ii) E_{strain} , which contains all the energy terms directly related to the strain tensor η ; (iii) E_{inter} , which contains several terms describing the two-body interactions between different local modes or the same local modes at different sites; and (iv) E_{spring} , which describes the effect of atomic configuration of different elements (known as “alloying effect”²²), which consists of several “spring” terms (using the terminology of ref. 28).

In principle, the formalism of effective Hamiltonian could be applied to any structures where a reference structure with high symmetry can be defined. Here, we only focus on the perovskites in formula ABX₃, in which A- or B-sites can be occupied by multiple elements. Practically, the local dipolar mode vector $\{u\}$, antiferrodistortive (AFD) pseudovector $\{\omega\}$, and inhomogeneous strain vector (acoustic mode) $\{v\}$ are considered as the

modes $\{s\}$ (see Fig. 1a, and in total nine degrees of freedom describe the state of each unit cell). More details of the effective Hamiltonian for perovskites are described in “Methods”.

Mode and basis

The mode is the local collective displacement of atoms in a specified pattern (see Fig. 1a), which could be either “local mode”⁷ or, more generally, “lattice Wannier function”^{29,30}. In the examples depicted in this work, the local mode is simply employed. As discussed in Sec. VI of the Supplementary Information, for simple perovskites like BaTiO₃, this simple local mode basis is sufficient to capture the soft phonon bands related to the onset of ferroelectricity. In perovskites, the local mode basis of dipole motion u is typically chosen to be the local phonon mode having Γ_{15} symmetry centered on A or B site²¹. Typically, the local mode basis is determined from the eigenvector associated with the dipolar mode of the force constant or dynamic matrix of cubic perovskite, which takes the form $\xi = (\xi_A, \xi_B, \xi_{X1}, \xi_{X2})$. For example, the displacement of local mode motion $u_{i\alpha}$ centered at B site consisting of the displacement of center B atom by amounts of $u_i \xi_B$, the displacement of eight neighbor A atom by amounts of $u_i \xi_A/8$, and the displacement of the six neighbor X atom by amounts of $u_i \xi_{X1}/2$ or $u_i \xi_{X2}/2$, all along the α direction. Note that it is also possible to get the local mode basis by fitting against the atomic displacement between the reference structure and low energy structure³¹. The local motion v is similar to u but with the basis corresponding to the translation motion of all the atoms in the unit cell, i.e. with $\xi_A = \xi_B = \xi_{X1} = \xi_{X2}$.

The AFD mode ω is kind of different from the u and v modes since a neighboring BX₆ octahedron shares the same X atom, and thus the ω modes are not completely independent from each other. The actual movement of the X atom shared by the i and j sites associated with the AFD mode is given by

$$\Delta \mathbf{r}_X = \frac{a_0}{2} \hat{\mathbf{R}}_{ij} \times (\omega_i - \omega_j), \quad (1)$$

where $\hat{\mathbf{R}}_{ij}$ is the unit vector jointing the site i and site j . By definition of Eq. (1), there are multiple (actually, infinite) different sets of $\{\omega\}$ modes representing the same atomic structure (i.e. with the same set of atomic displacement)³². For example, it is clear that adding an arbitrary amount of ω_0 to all of the AFD modes does not change the displacement $\Delta \mathbf{r}_X$, since the displacement only depends on the *difference* between ω_i and ω_j . To eliminate such arbitrariness, we typically impose the following extra restrictions on the

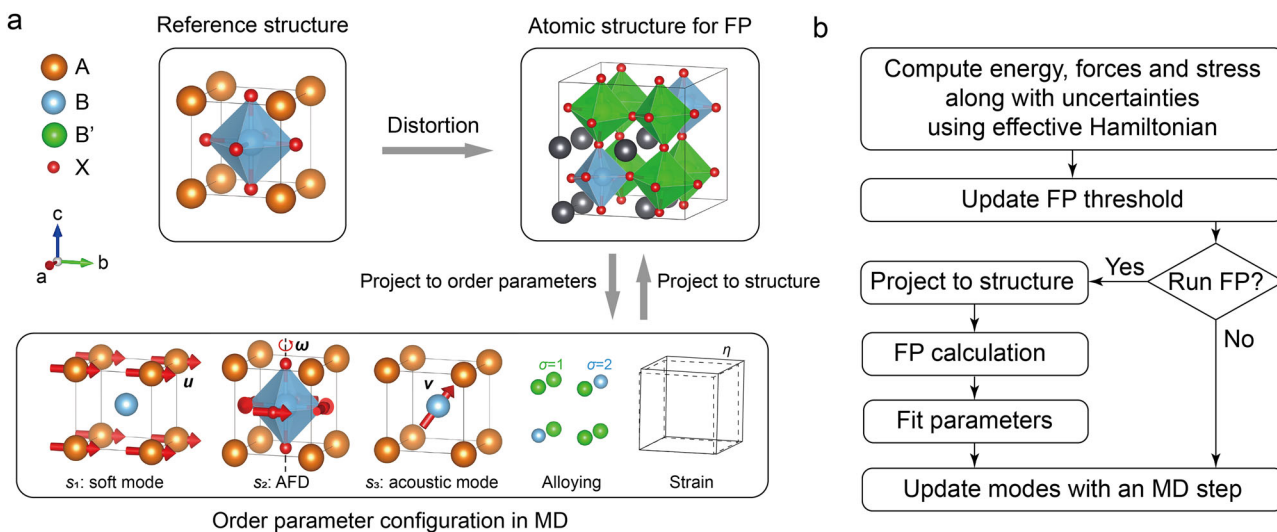


Fig. 1 | Schematics of on-the-fly learning of effective Hamiltonian for perovskite structure. **a** The projection between the atomic structure used in the FP calculations and the order-parameters configuration used in effective Hamiltonian MD simulations. **b** The workflow of on-the-fly learning of effective Hamiltonian.

AFD vectors and their cyclic permutations:

$$\forall x_0, \sum_{i, n_x(i)=x_0} \omega_{i,x} = 0, \quad (2)$$

where i is the index of unit centered at $n_x(i)\hat{x}a_0 + n_y(i)\hat{y}a_0 + n_z(i)\hat{z}a_0$, $\hat{x}, \hat{y}, \hat{z}$ are unit vectors along the x, y, z axes, and a_0 is the lattice constant of the five-atom perovskite unit cell. The summation runs over all the sites in the same layer marked with $n_x(i) = x_0$. Note that our definition of atomic displacement [Eq. (1)] is identical to that in ref. 32 [Eq. (1) there in], but our formalism is different from that of ref. 32 by the extra restrictions [Eq. (2)].

It is clear from above that all of the \mathbf{u} , \mathbf{v} , and $\mathbf{\omega}$ modes are linked *linearly* with atomic displacement about the reference structure. For a periodic supercell containing $N = L_x \times L_y \times L_z$ five-atom perovskite unit cells, the relation between the modes and atomic displacements could be written as

$$\mathbf{Ms} = \mathbf{x}, \quad (3)$$

where \mathbf{s} is a $9N$ column vector containing the modes \mathbf{u} , \mathbf{v} , $\mathbf{\omega}$ in each unit cell, \mathbf{x} is a $15N$ column vector containing the atomic displacement of each atom in the supercell, and \mathbf{M} is the matrix containing the information of local mode basis. The force acting on the *mode* could then be obtained from the chain rule

$$f_{s,i} = -\frac{\partial E_{\text{pot}}}{\partial s_i} = -\sum_j \frac{\partial E_{\text{pot}}}{\partial x_j} M_{ji}. \quad (4)$$

This equation can be written in matrix form as

$$\mathbf{f}_s = \mathbf{M}^T \mathbf{f}_x, \quad (5)$$

where \mathbf{f}_s and \mathbf{f}_x gather the forces acting on the modes and atoms, respectively.

Similar to the second-principle lattice dynamics formalism³³, the actual atomic coordinates in a supercell with homogeneous strain η and atomic displacement is defined as

$$\mathbf{r}_{lk} = (\mathbb{1} + \boldsymbol{\eta})(\mathbf{R}_l + \boldsymbol{\tau}_k) + \mathbf{x}_{lk}, \quad (6)$$

where $\mathbb{1}$ is the 3×3 identity matrix, $\boldsymbol{\eta}$ is the homogeneous strain (in 3×3 matrix format), \mathbf{R}_l is lattice vector corresponding to the unit cell l , $\boldsymbol{\tau}_k$ is the coordinate of the atom inside the unit cell. Thus, the stress compatible with that calculated from FP should be obtained using the chain rule

$$\sigma_m = -\frac{\partial' E_{\text{pot}}}{\partial' \eta_m} = -\frac{\partial E_{\text{pot}}}{\partial \eta_m} - \sum_{lk\alpha} \frac{\partial E_{\text{pot}}}{\partial x_{lk\alpha}} \frac{\partial x_{lk\alpha}}{\partial \eta_m}, \quad (7)$$

as described in Appendix A of ref. 33. Practically in this work, such relation is used *inversely*. The stress $-\partial' E_{\text{pot}}/\partial' \eta_m$ obtained from the FP calculations is converted to $-\partial E_{\text{pot}}/\partial \eta_m$, compatible with the direct definition of the effective Hamiltonian.

Formalism of the parametrization

Instead of doing many FP energy calculations on *special* structures with distortions to compute the coefficients of order-parameters coupling in effective Hamiltonian as in previous reports^{7,21}, our present approach is to use the on-the-fly active-learning approach to automatically compute the parameters for effective Hamiltonian. The parameters related to the long-range dipolar interaction E_{long} [Eq. (S6) in the Supplementary Information] [i.e. the lattice constant a_0 , the dipolar mode Born effective charge Z^* and optical dielectric constant ϵ_∞ (using the notations of ref. 7)] are first determined directly from first principles calculations. Then, all the remaining parameters are determined through an on-the-fly machine-learning process. As indicated in Methods, the effective Hamiltonian can be

written in the following form

$$E_{\text{pot}} = E_{\text{long}} + \sum_{\lambda=1}^M w_\lambda t_\lambda(\{\mathbf{u}\}, \{\mathbf{v}\}, \{\mathbf{\omega}\}, \{\sigma\}, \eta), \quad (8)$$

where E_{long} is fixed during the fitting process, M is the number of parameters to be fitted, w_λ is the parameter to be fitted, and t_λ is the energy term associated with the parameter w_λ , which is called symmetry-adapted term (SAT), using the terminology of ref. 33. In other words, except long-range dipolar interactions, the energy of the system is *linearly* dependent on the *parameters*. Moreover, the force (respectively, stress) has similar forms to the energy, which is obtained by taking derivative over local mode (respectively, strain) on E_{long} and t_λ . Such linearity is similar to the second-principle lattice dynamics³³ and MLFF with Gaussian approximation potential³⁴, allowing the application of similar regression algorithms. Here, we use the Bayesian linear regression algorithm similar to that previously used for MLFF², with several key modifications for the effective Hamiltonian context.

Given the linearity above, the linear parts of energy, force, and stress for each structure a calculated from the effective Hamiltonian could be written in the following matrix form

$$\tilde{\mathbf{y}}_a \equiv \mathbf{y}_a - \mathbf{y}^{\text{long}} = \boldsymbol{\phi}_a \mathbf{w}, \quad (9)$$

where \mathbf{y} is a vector containing the energy per unit cell with respect to the reference structure, the forces acting on the modes, and the stress tensor (in total $m_a = 1 + 9N_a + 6$ elements, where N_a is the number of unit cells in the structure a , and we consider the above mentioned nine local modes in our models), \mathbf{y}^{long} is a vector in similar layout associated with the E_{long} term, and \mathbf{w} is a vector that consists of all the parameters $w_\lambda, \lambda = 1, \dots, M$; and $\boldsymbol{\phi}_a$ is an $m_a \times M$ matrix consisting of the SATs and their derivatives with respect to modes and strain. Note that in the effective Hamiltonian formalism, the potential energy of the reference structure is zero by definition. Thus, the energy obtained from the FP calculations in \mathbf{y} should be subtracted by the energy of the reference structure to be consistent with the effective Hamiltonian.

In the parametrization process, a set of structures is selected as the training set (see “On-the-fly learning”), and the structures are indexed by $a = 1, \dots, N_T$. First-principles calculations are performed on these structures to get the energy per unit cell, forces acting on the atoms, and the stress tensor. The forces acting on the modes are then obtained by applying Eq. (5). The $\tilde{\mathbf{y}}_a$ vector of all the structures in the training set then constitutes the vector \mathbf{Y} containing $\sum a_m$ elements. On the other hand, the $\boldsymbol{\phi}_a$ matrices of the structures in the training set constitute the $\boldsymbol{\Phi}$ matrix. In this form, the parametrization problem is to adjust \mathbf{w} to fit $\boldsymbol{\Phi}\mathbf{w}$ against \mathbf{Y} . To balance the energy, force and stress values with different dimensions properly, they are typically divided by their standard deviation in the training set to get dimensionless values. Furthermore, an optional weight could be assigned to each of the types to adjust the preference between different fitting targets. Practically, this is achieved by left multiplying a diagonal matrix \mathbf{H} made up of h_i/σ_i to $\boldsymbol{\Phi}$ and \mathbf{Y} , where h_i and σ_i are the weight and standard deviation of the specified type of values (energy, force of different modes and stress), respectively.

Given two necessary assumptions satisfied (see Appendix B of ref. 2), the posterior distribution of the parameter is a multidimensional Gaussian distribution

$$p(\mathbf{w}|\mathbf{Y}) = \mathcal{N}(\bar{\mathbf{w}}, \boldsymbol{\Sigma}), \quad (10)$$

where the center of the distribution

$$\bar{\mathbf{w}} = \frac{1}{\sigma_v^2} \boldsymbol{\Sigma} \boldsymbol{\Phi}^T \mathbf{Y} \quad (11)$$

is the desired optimal parameters, and the variance

$$\Sigma = \left[\frac{1}{\sigma_v^2} \mathbf{I} + \frac{1}{\sigma_w^2} \Phi^T \Phi \right]^{-1} \quad (12)$$

is a measure of the uncertainty of the parameters. Here, \mathbf{I} is the identity matrix, σ_v is a hyperparameter describing the deviation of FP data from the model prediction $\phi_{\alpha} \mathbf{w}$, and σ_w is a hyperparameter describing the covariance of the prior distribution of parameter vector \mathbf{w} (see Appendix B of ref. 2 for more details).

Given the observation of the training set, the posterior distribution of the energy, forces, and stress of a new structure is also shown to be a Gaussian distribution²

$$p(\bar{\mathbf{y}}|\mathbf{Y}) = \mathcal{N}(\bar{\mathbf{w}}, \sigma), \quad (13)$$

where the covariance matrix

$$\sigma = \sigma_v^2 \mathbf{I} + \Phi \Sigma \Phi^T \quad (14)$$

measures the uncertainty of the prediction of the new structure. Following ref. 2, the diagonal elements of the second term is used as the Bayesian error. If the Bayesian error is large, the prediction on the energy, forces, and stress by the current effective Hamiltonian model is considered unreliable, then a new FP calculation is required to fit the parameters.

The hyperparameters σ_v and σ_w are determined by evidence approximation², in which the marginal likelihood function corresponding to the probability of observing the FP data \mathbf{Y} with σ_v and σ_w is maximized [see Eq. (31) and Appendix C in ref. 2]. Practically, the hyperparameters σ_v and σ_w are calculated along with Σ and $\bar{\mathbf{w}}$ by executing self-consistent iterations at each time when FP data for a new structure is collected.

The Bayesian linear regression described above is equivalent to the ridge regression^{5,35} in which the target function

$$\mathcal{O} = \|\Phi \mathbf{w} - \mathbf{Y}\| + \lambda \|\mathbf{w}\|^2 \quad (15)$$

is minimized, where λ is the Tikhonov parameter which is equivalent to σ_v^2/σ_w^2 here^{5,35}. The main purpose of imposing the Tikhonov parameter is to prevent overfitting³⁵. However, in the context of effective Hamiltonian parametrization, there are only a small amount of parameters to be determined (typically from several tens to over a hundred), while the number of values collected from FP calculations is typically much larger, which means the linear equations $\Phi \mathbf{w} = \mathbf{Y}$ is greatly over-determined. In such case, the regularization is usually not necessary. If the regularization term $\lambda \|\mathbf{w}\|^2$ in Eq. (15) is removed, the problem becomes a simple linear least square fitting, and the parameter could be simply solved by

$$\mathbf{w} = \Phi^+ \mathbf{Y}, \quad (16)$$

where Φ^+ is the Moore-Penrose pseudoinverse of the matrix Φ , which could be computed by performing the singular-value decomposition of Φ ³⁶. Indeed, our numerical tests show that the resulting parameter from such fitting without regularization is pretty close to that obtained by Bayesian linear regression. Similar observation is also reported in the context of MLFF with Gaussian approximation potential model (or its analogs)³⁶. On the other hand, in effective Hamiltonian, unlike Gaussian approximation potential, the parameters in \mathbf{w} have different dimensions, and it is hard to balance the *values* between different parameters, indicating that the regularization may be not suitable for effective Hamiltonian. Based on the two reasons above, in our fitting scheme, it is typically assumed that $\sigma_w \rightarrow \infty$, and thus the equivalent Tikhonov regularization parameter λ approaches zero, and the fitting scheme is equivalent to the linear least square fitting.

On-the-fly learning

In our approach, the parameters of effective Hamiltonian are fit in a scheme similar to that generating on-the-fly machine-learning force field (MLFF)² with some modifications for the effective Hamiltonian scheme. The parameters are fitted during effective Hamiltonian MD simulations on relatively small cells. The effective Hamiltonian MD simulations are performed by solving the equations of motions of each degree of freedom

$$\begin{aligned} \frac{\partial p_i}{\partial t} &= -\frac{\partial E_{\text{pot}}}{\partial s_i}, \\ \frac{\partial s_i}{\partial t} &= \frac{p_i}{m_i}, \end{aligned} \quad (17)$$

where p_i is the momentum associated with the degree of freedom s_i ; m_i is the effective mass of the degree of freedom s_i ; and t is the time. In this work, the effective mass of the degrees of freedom is obtained by taking the weighted average mass of the cooperated atoms according to the square of their normalized distortion amplitudes in the basis, as in ref. 37. Note that there are also some other strategies for choosing the effective masses, for example, fitting against the phonon frequencies as in ref. 31. As shown in Fig. 1b, in each MD step, the energy, forces and stress tensor on the structure as well as their uncertainties are predicted by the effective Hamiltonian with the current parameters and collected data using the Bayesian linear regression. If the uncertainty (Bayesian error) of the energy, forces, or stress tensor is large, the FP calculation is executed, the corresponding results are stored in the training set, and the parameters are refitted using the updated training set; otherwise, the FP calculation is skipped. Then, the structure is updated by executing one MD step with the forces and stress from the FP calculation (if available) or those from the effective Hamiltonian.

During the fitting process, the Bayesian errors of the energy, forces and stress predicted by the effective Hamiltonian are calculated by Eq. (14) and compared to the threshold to determine whether FP calculation is necessary. At the beginning, the threshold is typically initialized with zero. Before the setting up of the non-zero threshold, the FP calculations take place in a fixed interval of several steps (say, 10 or 20 MD steps). The threshold is then updated dynamically during the fitting process using the flow similar to that in ref. 2, with the exception that the spilling factor is not used in this work. Note that different from ref. 2, the parameters are typically fitted *immediately* as soon as the new FP calculation is finished, instead of fitted after several FP results are obtained. This difference stems from the observation that the parameter fitting for the effective Hamiltonian is typically very fast compared to the FP calculations. Such immediate fitting is helpful for reducing the required number of FP calculations and improving the fitting efficiency.

Applications

Simple perovskite BaTiO₃. The on-the-fly learning effective Hamiltonian is first applied to simple perovskite BaTiO₃, which is one of the most studied ferroelectric perovskites. Figure 2a, b, and c show the parameter evolutions during on-the-fly machine learning. The simulation is performed on $2 \times 2 \times 2$ supercell (40 atoms) at the temperature of 50 K. The Bayesian error during the fitting process is displayed in Fig. 2a. At the beginning (about 500 steps), the Bayesian error is quite large, and FP calculations are called frequently. As the fitting progresses, more FP data is collected, and the parameters are updated, leading to the rapid decline of Bayesian error. The threshold is also adjusted dynamically in this process. After about 1000 MD steps, the threshold is nearly unchanged and the FP calculations are only rarely required. Figure 2b shows the potential energy predicted by the effective Hamiltonian and that computed from FP calculations in the simulation, showing they are close to each other at each step. Figure 2c shows the mode evolution during the simulation. In the range shown in Fig. 2a–c, about 35000 MD steps are taken, and only 36 FP calculations are performed. The fitting process is further taken on $2 \times 4 \times 4$ supercell (160 atoms) to get the parameters corresponding to Fig. 2d, e.

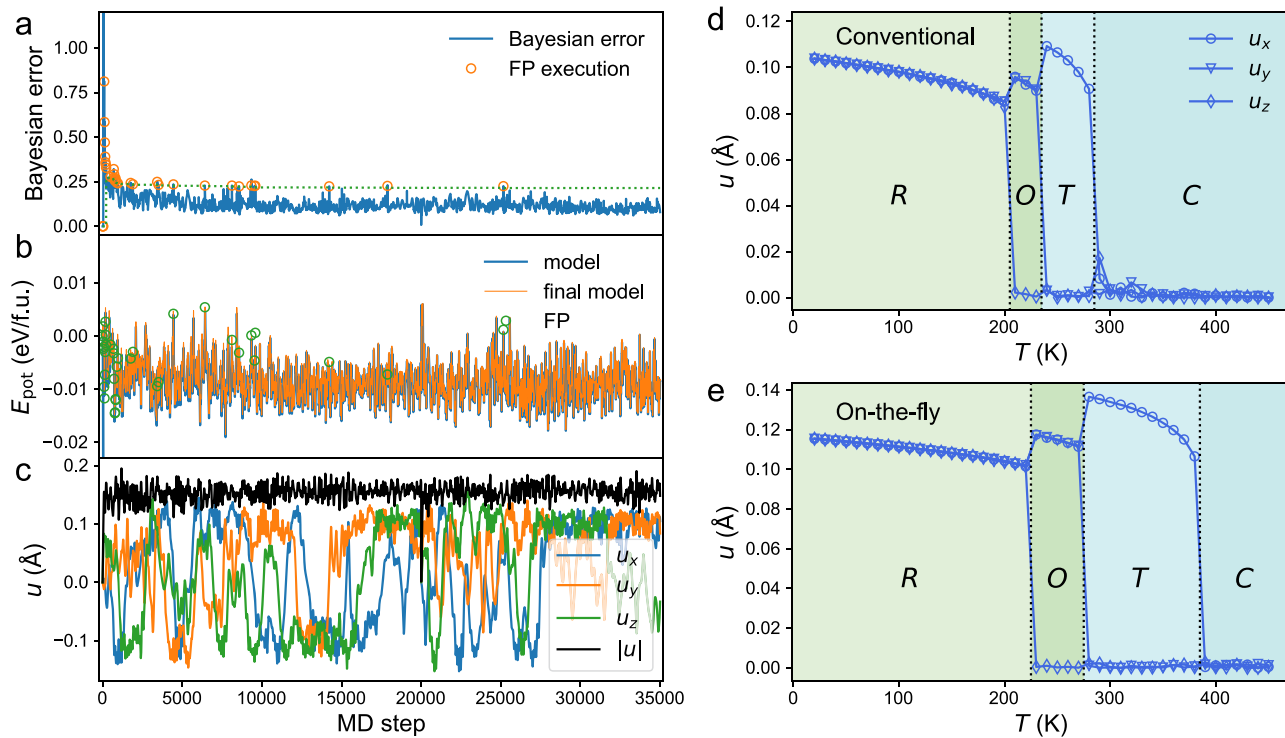


Fig. 2 | On-the-fly machine learning of parametrization for BaTiO₃. a–c—(a) Bayesian error, (b) potential energy per formal unit (f.u.), and (c) local dipolar mode \mathbf{u} in the learning/fitting process as functions of MD steps. The dash line in panel (a) denotes the threshold to perform FP calculations. The blue and orange lines in panel (b) represent the energy computed by effective Hamiltonian model during the fitting process and with the final parameter after the learning process, respectively.

Phase diagram by effective Hamiltonian simulations with the parameters from (d) direct FP calculations using the method in ref. 7 and (e) on-the-fly learning. Absolute values of local mode \mathbf{u} of BaTiO₃ as functions of temperature are shown in panel (d), (e). Here, R, O, T, and C denote the rhombohedral, orthogonal, tetrahedral, and cubic phases, respectively.

Figure 2d, e show the phase diagrams of BaTiO₃ obtained from the effective Hamiltonian simulation with parameters from the conventional parameterization and from on-the-fly learning, respectively. The supercell size is chosen to be 12 × 12 × 12 (corresponding to 8640 atoms). At high temperatures, all components of the dipolar mode are zero, characterizing a paraelectric cubic (C) phase. With the decreasing of temperature, the C phase sequentially transforms into ferroelectric tetrahedral (T), orthogonal (O), and rhombohedral (R) phases, characterized by one, two, and three non-zero components of the dipolar mode, respectively. Such C-T, T-O, and O-T phase transition sequences simulated by the effective Hamiltonian with both sets of parameters are correctly reproduced and are consistent with experimental results⁷⁹. For the calculations with the parameters from conventional FP calculations (Fig. 2d), the C-T, T-O, and O-T phase transition temperatures are about 280, 230, and 200 K, respectively. While for the calculation with on-the-fly learning parameters, they are 380, 270, and 220 K, respectively, much closer to the experimental values of 403, 278, and 183 K, respectively⁹. Note that such improvement of critical temperature mainly originates from the inclusion of new anharmonic intersite interactions. More precisely, it is found that the following two terms play important roles in the improvement of phase transition temperatures, namely,

$$E_{\text{inter},u^3-u^1,2} = K_2^{u^3-u^1} \left(u_{i,z}^2 u_{i,y} u_{i+z,y} + \text{symmetrically equivalent terms} \right), \quad (18)$$

and

$$E_{\text{inter},u^3-u^1,5} = K_5^{u^3-u^1} \left(u_{i,x}^2 u_{i,y} u_{i+z,y} + \text{symmetrically equivalent terms} \right), \quad (19)$$

where $u_{i,x}$ indicates the x component (here the x, y, z Cartesian coordinates are along the pseudocubic [100], [010], [001] directions, respectively) of the local dipolar mode at the unit cell indexed i , $u_{i+z,y}$ indicates the y component of the dipolar mode at the neighbor unit cell of i with relative position vector $a_0 \hat{z}$ (where a_0 is the lattice constant of the five-atom perovskite unit cell, and \hat{z} is the unit vector along the z direction). For simplicity, only one representative product is given for each of the two terms, with other (11 for each) symmetrically equivalent terms omitted. Such terms could be understood as “transverse” modification to the interaction between parallel local dipolar modes (see Fig. S3 in the Supplementary Information) at finite temperatures, making the ferroelectric phase more stable and thus improving the prediction of the phase transition temperatures. A more detailed discussion is given in the Supplementary Information.

Multidomain PbTiO₃. The on-the-fly learning approach is then applied to the ferroelectrics PbTiO₃ to investigate the domain wall structure. It was previously reported³⁸ that the multidomain PbTiO₃ could exhibit Bloch feature in the domain wall. To investigate the domain wall structure with our effective Hamiltonian scheme, the multidomain PbTiO₃ with a Bloch-like domain wall is built (Fig. 3a). After the simulated annealing using the effective Hamiltonian, we obtain the configuration depicted in Fig. 3b, c. The local dipolar mode (directly proportional to local polarization) is along the x -axis in both domains. Near the domain wall, the magnitudes of the x component of the dipolar mode decrease and are then reversed. Meanwhile, the y component of local dipolar mode is almost zero in both domains, while it shows relatively significant values in the domain wall. Such changes in the local dipolar mode show a Bloch-like character in the domain wall, which is qualitatively consistent with what was previously reported. Note, however, that there are some quantitative differences from the cited work. More specifically, in ref. 38, the polarization (along the y direction) in the domain wall is comparable

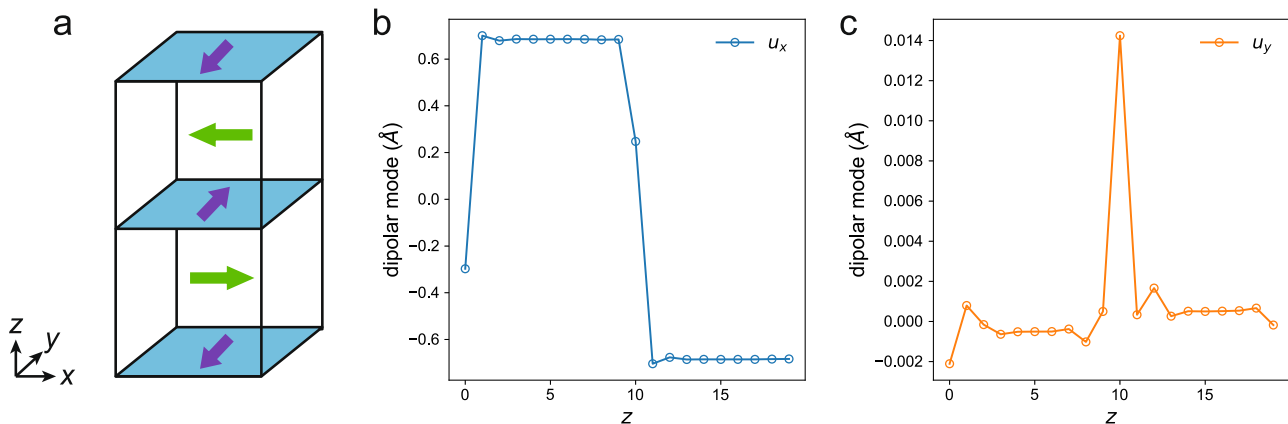
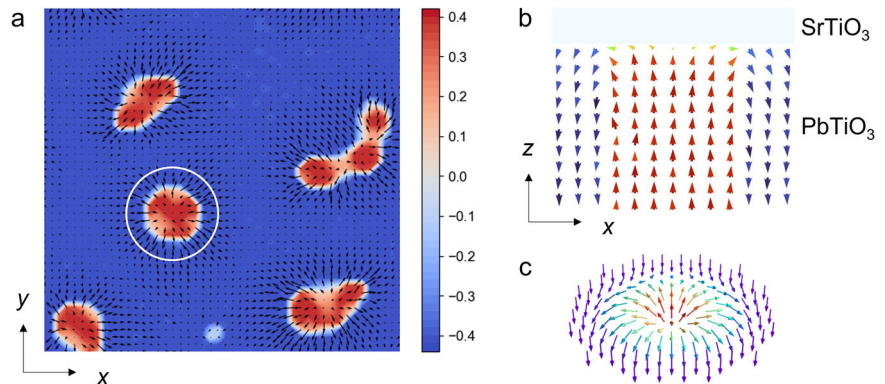


Fig. 3 | Dipolar mode distribution for a PbTiO_3 multidomain with domain walls. a Initial configuration. Here, the blue planes refer to the domain walls, the green and purple arrows indicate the polarization directions in the domains and the domain

walls, respectively. b x -component of local dipolar mode in the configuration after simulated annealing, as a function of position along the z -axis (in the unit of five-atom perovskite unit cell). c Same as b, but for the y -component.

Fig. 4 | Polar distribution of $\text{SrTiO}_3/\text{PbTiO}_3$ bilayer. a Dipole configuration of $\text{SrTiO}_3/\text{PbTiO}_3$ averaged over the top 10 planes of PbTiO_3 layer obtained from HMC simulation with the effective Hamiltonian. The arrows denote the in-plane component of the local dipolar mode, and the colors denote the out-of-plane components of dipolar modes. b The dipole configuration of $\text{SrTiO}_3/\text{PbTiO}_3$ in a (010) plane around the circled skyrmion in panel (a). The colors of the arrows denote the out-of-plane component of the local dipolar mode. c The schematic of the skyrmion at the top of the PbTiO_3 layer, where the color of the arrows denotes the out-of-plane component of local dipolar mode.



to that in the domain, while in this work, the polarization in the domain wall is much smaller than that in the domain. Such difference may be attributed to the reduced degrees of freedom of the effective Hamiltonian, and/or some details of the physical conditions of the simulation (for example, the starting temperature of the simulated annealing simulation, the size of the supercell, etc.) or some details of the construction of our model (for example, the local mode basis, fitting configurations or even details of the employed FP method). While the detailed investigation into these conditions remains for another work, it is remarkable that our on-the-fly learning scheme—with MD simulations restricted to relatively small supercells and no explicit consideration of ferroelectric domain walls—already captures the essential Bloch character of this boundary.

Solid-solution $\text{Pb}(\text{Zr}_{0.75}\text{Ti}_{0.25})\text{O}_3$. The on-the-fly learning approach is then applied to the solid solution of ferroelectric $\text{Pb}(\text{Zr}_{1-x}\text{Ti}_x)\text{O}_3$, which is of great interest because of its high piezoelectricity and widespread applications³⁹. We choose the solid solution of $\text{Pb}(\text{Zr}_{1-x}\text{Ti}_x)\text{O}_3$ ($x = 0.25$) (PZT25) to demonstrate our on-the-fly learning effective Hamiltonian. The active learning is performed on PZT25 using $2 \times 2 \times 2$ and $2 \times 4 \times 4$ (40 and 160 atoms, respectively) with random arrangements of Ti and Zr atoms (see Supplementary Information). Using the parameters from this active learning, effective Hamiltonian calculations with supercell of $12 \times 12 \times 12$ show that PZT25 possesses cubic (C), rhombohedral with space group $R3m$, and rhombohedral with space group $R3c$ phases as the temperature decreases from 700 K to 20 K, with the transition temperature around 540 K (C- $R3m$) and 340 K ($R3m$ - $R3c$) (see Fig. S4 in the Supplementary Information), very close to the experimental values of

593 K (C to $R3m$) and 390 K ($R3m$ to $R3c$)⁴⁰, indicating the validity of our on-the-learning scheme for solid-solution structures.

Polar skyrmion-like nanodomains. The emergent and exotic phases of polar topological configurations, such as polar skyrmions, have garnered enormous interest in condensed-matter physics. Most polar topological configurations were found near the interface of polar superlattices or heterostructures^{19,41}. Here, we find polar skyrmion in $\text{SrTiO}_3/\text{PbTiO}_3$ bilayer by our on-line-fly learning effective Hamiltonian.

The structure of PbTiO_3 with surface capping by a few SrTiO_3 layers is considered. Supercell of $48 \times 48 \times 48$ with 43 PbTiO_3 layers, 5 SrTiO_3 layers, and vacuum layers along the z direction is used. The parameters of the effective Hamiltonian are obtained by performing our on-the-fly learning approach on $(\text{Pb}_{7/8}\text{Sr}_{1/8})\text{TiO}_3$ solid solutions with random arrangements of Pb and Sr atoms. Figure 4a shows the local dipole configuration averaged over the top 10 PbTiO_3 layers obtained from hybrid Monte Carlo (HMC) simulations at 10 K. One can clearly see that there are topological upwards-oriented nanodomains embedded in a downwards-oriented matrix. The in-plane polarization within such nanodomains has a center-divergent character with the two-dimensional winding number equal to one of each domain^{19,42}. Figure 4b shows the local dipoles in (010) plane of the nanodomain delimited by white circle of Fig. 4a, indicating the center-divergent polar skyrmion-like nanodomain (see the sketch in Fig. 4c). Note that such polar skyrmion-like nanodomain is consistent with the experimental findings, as show in Sec. IX in the Supplementary Information. The above simulation and verification confirm the validity of our on-the-fly learning effective Hamiltonian approach for such complex interaction and complex system.

Discussion

To demonstrate the computational efficiency of our effective Hamiltonian methods, we compare the time consumed by the effective Hamiltonian MD with other methods, such as deep potential MD⁴³, MLFF MD, and ab initio MD simulations². As shown in Fig. 5, the time consumed by ab initio MD simulations increases drastically with the increase of supercell size, and is much slower than other methods, as consistent with common beliefs. The time spent by other methods increases slowly with the increase of supercell size within a similar slope in the log-log scale. For the same supercell size, the time spent by effective Hamiltonian simulation is less than the deep potential MD and MLFF MD by about 3 orders of magnitude, respectively. Notably, the size of the investigated structure by the effective Hamiltonian here is up to $128 \times 128 \times 128$ supercells, corresponding to 10485760 atoms, with only one CPU core. The time spent by effective Hamiltonian simulation shows a nearly linear dependency on the number of atoms in the log-log scale with a slope of about 1.036 as obtained from linear fitting. Such a result indicates that, numerically, the consumed time t_{MD} scales nearly linearly with respect to the number of atoms N_{at} as $t_{\text{MD}} \approx CN_{\text{at}}^{1.036}$, where C is a constant. Note that the theoretical asymptotic time complexity should be $O(N_{\text{at}} \log_2 N_{\text{at}})$ ⁴⁴, in reasonable consistent with the numerical result. Note that these methods possess similar accuracy as they are all based on FP calculations. Although the effective Hamiltonian method only includes 6 ionic degrees of freedom in each five-atom perovskite unit cell (i.e., the local dipolar mode $\{\mathbf{u}_i\}$ and inhomogeneous strain variable $\{\mathbf{v}_i\}$, each containing three degrees of freedom per unit cell) while the other methods include full sets of 15 degrees of freedom, all of these methods capture the most important distortions related to the ferroelectric phase transitions.

It is worth noting that in some previous MLFF or second-principles works, the parameters are fitted against some pre-generated distorted structures. For example, AIMD trajectories are used in ref. 33. In fact, we have also tried to fit the effective Hamiltonian using the trajectories generated from AIMD, but the resulting parameters are not accurate (as they could not reproduce some important phase transitions) and show a strong dependency on the choice of AIMD conditions (for example, the starting configuration of AIMD simulations; the temperature of AIMD simulation, etc). This fact indicates that the effective Hamiltonian parameters are rather sensitive to the training set, and the pre-generated dataset must be constructed with special care. In this sense, active-learning strategies are preferred.

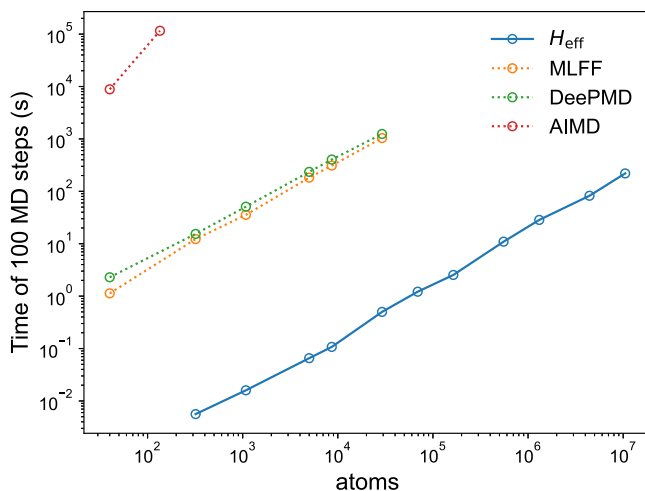


Fig. 5 | Computational time for 100 MD steps calculations as a function of the number of atoms in the simulated BaTiO_3 supercell, using the effective Hamiltonian (H_{eff}), MLFF, deep potential MD, and ab initio MD (AIMD). The tests are performed on the Intel(R) Xeon(R) Silver 4210R CPU using one core, except for the AIMD simulation, which is performed on the Intel(R) Xeon(R) CPU E5-2680 v3 CPU using 24 cores.

In summary, an on-the-fly active-learning scheme is developed to obtain the parameters of the effective Hamiltonian methods. The parameters are computed during MD simulations. The energy, forces, and stress, as well as their Bayesian errors, are computed at each MD step based on the effective Hamiltonian, and FP calculations are called to fit the parameters when the Bayesian errors are large. Typically, very few FP calculations are required in this process (usually much less than 1% of the total MD steps). The fitting procedure based on Bayesian linear regression provides not only the values of the parameters but also their uncertainties. Such a learning scheme offers a new way with high precision to parametrize the effective Hamiltonian in a universal and automatic process and is especially highly applicable for systems that have complex interactions in complex systems.

Methods

Effective Hamiltonian for perovskites

In the effective Hamiltonian of perovskites, the local modes $\{\mathbf{s}_i\}$ include the following types (1) the local dipolar mode \mathbf{u}_i in each five-atom perovskite unit cell i , which is directly proportional to the local electric dipole in unit cell i ; (2) the pseudovector \mathbf{w}_i centered at B site, characterizing the BX_6 octahedral tilting, also known as antiferrodistortive (AFD) distortions⁴⁵; and (3) the local variable \mathbf{v}_i characterizing the inhomogeneous strain around the unit cell i . Note that the \mathbf{u}_i and \mathbf{v}_i vectors could be chosen to be centered at either A site or B site for different materials. The potential energy of perovskites contains four main parts

$$E_{\text{pot}} = E_{\text{single}}(\{\mathbf{u}_i\}, \{\mathbf{w}_i\}, \{\mathbf{v}_i\}) + E_{\text{strain}}(\{\mathbf{u}_i\}, \{\mathbf{w}_i\}, \{\mathbf{v}_i\}, \eta) + E_{\text{inter}}(\{\mathbf{u}_i\}, \{\mathbf{w}_i\}, \{\mathbf{v}_i\}) + E_{\text{spring}}(\{\mathbf{u}_i\}, \{\mathbf{w}_i\}, \{\mathbf{v}_i\}, \{\sigma_i\}). \quad (20)$$

The first two terms E_{single} and E_{strain} contains mainly the terms already reported in previous effective Hamiltonian works^{7,12} (with a small amount of extension, see the Supplementary Information for more details). The last two terms E_{inter} and E_{spring} are different from previous works (see, e.g., refs. 45–47). Such terms are derived directly from symmetry here, making them more general, and the accuracy of the effective Hamiltonian can then be improved systematically.

The E_{inter} in Eq. (20) contains several two-body interaction terms that take the following form

$$E_{\text{inter}}^{pq} = \sum_{ijab} p_a(\mathbf{R}_i) q_b(\mathbf{R}_j) K_{ab}(\mathbf{R}_i - \mathbf{R}_j), \quad (21)$$

where \mathbf{R}_i and \mathbf{R}_j are the position of the sites indexed by i and j , p and q are two variables participating in this interaction, and a, b are their subscripts. The interaction matrix $K_{ab}(\mathbf{R}_i - \mathbf{R}_j)$ contains the symmetry and parameter of the interaction. The specific form of the interaction matrix is determined by finding the symmetry invariant terms under the symmetry operations of the reference structure (see ref. 48). This interaction term [Eq. (21)] may be either long-ranged or short-ranged. For long-range interactions, both the i and j indexes run over all the sites in the simulated supercell. On the other hand, for short-range interactions, the i index runs over all the sites in the simulated supercell, while the j runs over the neighbor sites around i (within certain range for each type of interaction). In such a case, the interaction matrix is localized. Note that, the interaction variable p, q here could be not only the primitive degrees of freedom (i.e. $\mathbf{u}, \mathbf{v}, \mathbf{w}$), but also their onsite direct products. For example, the 6-dimension vector \mathbf{U} expressing the onsite direct product of $\mathbf{u} \otimes \mathbf{u}$ with subscript a being Voigt notation ($U_1 = u_x^2, U_4 = u_y u_z$) could be a valid interaction variable in Eq. (21). Throughout this article, the expression “ $p^m - q^n$ interaction” denotes the interaction that includes m th order contribution from p and n th order contribution from q . For example, the “ $u^1 - \omega^2$ interaction” is the interaction that equivalent to

$$E_{\text{inter}}^{u^1 - \omega^2} = \sum_{ijab\beta} u_a(\mathbf{R}_i) \omega_\beta(\mathbf{R}_j) \omega_\gamma(\mathbf{R}_j) K_{\alpha\beta\gamma}(\mathbf{R}_i - \mathbf{R}_j). \quad (22)$$

As in previous MD and HMC works⁴⁴, the interaction in Eq. (21) could be handled in the reciprocal space by using fast Fourier transformation to improve the computational efficiency.

The detailed interaction terms that are used in this work are listed in the Supplementary Information. A brief discussion about the “inhomogeneous strain” η introduced in previous works^{7,12} is also given in the Supplementary Information.

The E_{spring} term in Eq. (20) consists of several so-called “spring” terms that take the following form

$$E_{\text{spring}}^p = \sum_{ij} p_a(\mathbf{R}_i) J_a(\sigma_j, \mathbf{R}_j - \mathbf{R}_i), \quad (23)$$

where p is variable [like that in Eq. (21)] that can be primitive local modes (\mathbf{u} , \mathbf{v} , $\mathbf{\omega}$) or their onsite direct products, and $J_a(\sigma_j, \mathbf{R}_j - \mathbf{R}_i)$ is the interaction matrix containing the symmetry and parameter that depending on the occupation on site j and the position difference between i and j sites. To determine the specific form of J matrix, the σ variable is treated as an onsite scalar variable that is invariant under any symmetry operations. Then, the interactions allowed by symmetry are found by performing symmetry operations (of the reference structure space group) on the products $p(\mathbf{R}_i) \sigma(\mathbf{R}_j)$ and finding the invariant terms under such operations. Practically, the following spring interactions are considered: (1) The spring interaction of \mathbf{u} of first, second, and third order. (2) The spring interaction of \mathbf{v} of first order. (3) The spring interaction of $\mathbf{\omega}$ with second order. Note that for both the cases of multi A- or B-site element (i.e., the σ variables are centered on A- or B-site) and ω centering on B site, the first order of spring interaction is forbidden by symmetry. Thus, the second-order interaction is the lowest-order one. A brief discussion about the relations and differences of the treatment of “alloying effect” (using the terminology of ref. 22) between previous works and current work is given in the Supplementary Information.

Note that, for specified materials, some of the above terms may not be used since their effects are not important.

Computational details

On-the-fly machine learning for parametrization of effective Hamiltonian is performed on $2 \times 2 \times 2$ or $2 \times 4 \times 4$ supercells (corresponding to 40 or 160 atoms). The MD simulations are performed with isothermal-isobaric (NPT) ensemble using Evans-Hoover thermostat⁴⁹. Typically, each MD simulation on a given structure is executed for 20 ps to 200 ps. For each MD step, the FP calculation is required by the on-the-fly machine-learning process, and first-principles self-consistent calculation within density functional theory (DFT) is performed. All the FP calculations are performed using the VASP package⁵⁰ with the projector augmented wave (PAW) method. The solid-revised Perdew-Burke-Ernzerhof (PBEsol)⁵¹ functional is used. The $3 \times 3 \times 3$ and $3 \times 2 \times 2$ k-point meshes are used for the supercells with 40 and 160 atoms, respectively, and the plane wave cutoff of 550 eV is employed. The optical dielectric constant is computed using the density functional perturbation theory (DFPT)⁵². The Born effective charge of the local mode is obtained by fitting the polarization against the local mode amplitude, where the polarization is computed using the Berry phase method⁵³.

The phase transition simulations are conducted by Monte Carlo (MC) simulations with Metropolis algorithm⁵⁴ or hybrid MC algorithm⁴⁴ (HMC) with the effective Hamiltonian method. Each HMC sweep consists of 40 MD steps. Supercells of $12 \times 12 \times 12$ (corresponding to 8640 atoms) are used unless specially noted. For the phase transition simulations, the systems are cooled down from high temperatures (450 K and 700 K for BaTiO₃ and PZT25, respectively) to 20 K with relatively small temperature steps of 10 K.

In the MD and MC simulations, the following quantities are computed: (i) the average dipolar mode defined as $\mathbf{u} = \frac{1}{N} \sum_i \mathbf{u}_i$, (ii) the average

amplitude of dipolar mode defined as $|\mathbf{u}| = \frac{1}{N} \sum_i |\mathbf{u}_i|$, and (iii) the AFD at R point defined as $\omega_R = \frac{1}{N} \sum_i \omega_i (-1)^{n_x(i)+n_y(i)+n_z(i)}$.

In the study of BaTiO₃, the dipolar mode $\{\mathbf{u}_i\}$ is chosen to be centered at B site, the inhomogeneous strain variable $\{\mathbf{v}_i\}$ is chosen to be centered at A site, and the AFD $\{\omega_i\}$ variables are frozen at zero since they are not important in BaTiO₃. Such configuration of the degrees of freedom is consistent with previous works⁷. In the effective Hamiltonian, the dipolar mode onsite energy [Eq. (S2)] is considered up to the quartic order, the elastic energy [Eq. (S4)] is considered up to the quadratic order, and the $\eta - \mathbf{u}$ interaction is considered only up to the first term in Eq. (S5). The $2 \times 2 \times 2$ and $2 \times 4 \times 4$ supercells (corresponding to 40 and 160 atoms, respectively) are used in turn for on-the-fly learning. The parameters associated with Fig. 2d are obtained using conventional method^{7,21} with PBEsol functional. The j_5 and j_7 parameters (see ref. 7) are set to zero, as in ref. 55. For the phase transition simulations, negative pressure of -3 GPa is applied for both models (Fig. 2d, e) to correct the possible underestimation of the lattice constant by the DFT calculations.

In the study of PbTiO₃, the dipolar mode $\{\mathbf{u}_i\}$ is chosen to be centered at A site, the inhomogeneous strain variable $\{\mathbf{v}_i\}$ is chosen to be centered at B site, and the AFD $\{\omega_i\}$ variables are frozen at zero since they are not important in PbTiO₃. Such configuration of the degrees of freedom is consistent with previous works³¹. The local mode basis is chosen by fitting the atomic displacement between the cubic reference structure and the ferroelectrics tetrahedral structure. In the effective Hamiltonian, the dipolar mode onsite energy [Eq. (S2)] is considered up to the quartic order, the elastic energy [Eq. (S4)] is considered up to the quadratic order, and the $\eta - \mathbf{u}$ interaction is considered only up to the first term in Eq. (S5). The $2 \times 2 \times 2$ and $2 \times 4 \times 4$ supercells (corresponding to 40 and 160 atoms, respectively) are used in turn for on-the-fly learning.

The domain wall structure is simulated using a $12 \times 12 \times 20$ supercell (corresponding to 14400 atoms). The simulated annealing process starts from an HMC simulation at a relatively low temperature, followed by a sequence of MD simulations with decreasing temperature down to 1×10^{-7} K. The negative pressure of -6 GPa is applied to correct the potential underestimation of the lattice constant by the FP calculations.

In the study of PZT25, the local dipolar mode $\{\mathbf{u}_i\}$ is chosen to be centered at A site, the inhomogeneous variable $\{\mathbf{v}_i\}$ and the AFD pseudovector $\{\omega_i\}$ are centered at B site. The variable $\{\sigma_i\}$ is introduced to describe the occupation of Zr and Ti atoms at B site, where $\sigma_i = 1, 2$ denote Ti, Zr atom sit at the B site indexed by i , respectively. The dipolar mode onsite energy is expanded up to the fourth order. The spring interaction of \mathbf{u} is considered up to the third order and the nearest neighbor, the spring interaction of \mathbf{v} is considered up to the first order and second nearest neighbor, and the spring interaction of ω is considered up to the second order (which is the symmetry-allowed interaction of the lowest order) and the nearest neighbor. The Zr and Ti atoms are distributed randomly in the simulated supercells.

In the study of SrTiO₃/PbTiO₃ bilayer, the effective Hamiltonian is fitted to (Pb_{7/8}Sr_{1/8})TiO₃ solid solutions. The local dipolar mode $\{\mathbf{u}_i\}$ is chosen to be centered at A site, the inhomogeneous variable $\{\mathbf{v}_i\}$ and the AFD pseudovector $\{\omega_i\}$ are centered at B site. The variable $\{\sigma_i\}$ is introduced to describe the occupation of Pb and Sr atoms at A site, where $\sigma_i = 1, 2$ denote Pb, Sr atom sit at the A site indexed by i , respectively. The local mode basis of the local dipolar mode is obtained from fitting against the atomic distortion between the ferroelectric tetrahedral phase and the cubic perovskite phase. The dipolar mode onsite energy is expanded up to the fourth order. The spring interaction of \mathbf{u} is considered up to the third order and the nearest neighbor, the spring interaction of \mathbf{v} is considered up to the first order, and first nearest neighbor, and the spring interaction of ω is considered up to the second order (which is the symmetry-allowed interaction of the lowest order) and the nearest neighbor. The Pb and Sr atoms are distributed randomly in the supercell during the fitting process. The SrTiO₃/PbTiO₃ bilayer is modeled by $48 \times 48 \times 48$ supercell (corresponding to approximately 552960 atoms) that consists of 43 unit cell layers of PbTiO₃.

and 5 unit cell layers of SrTiO_3 along the z -axis, where periodic boundary condition is induced in x , y axes but not z -axis. Both (001) bilayers are terminated with A site layer. An epitaxy strain of -0.58% is imposed to mimic the SrTiO_3 substrate. The local configuration of Fig. 4a, b is obtained from a quench simulation (fast cool from 410 K to 10 K with temperature step of 100 K and 5000 HMC sweeps at each temperature).

In the computational efficiency tests for Fig. 5, the effective Hamiltonian simulation is conducted with one CPU core on different supercell sizes of BaTiO_3 for 10000 steps, the average time spent by each MD step is then calculated (with the initial preparation time excluded). For each size of a supercell, such process is repeated 5 times to get the average time. The MLFF simulation is performed using the VASP² package version 6.4.2. The force field for BaTiO_3 is first trained within $2 \times 2 \times 2$ supercell (40 atoms) at 300 K using 10000 MD steps. In this process, 461 local reference structures are collected. Then, it is switched to the prediction-only mode (ML_MODE=run) after refitting the field (with ML_MODE=refit) to measure the consumed time. For each supercell size, the simulation is performed with 1 CPU core for 100 MD steps, and the consumed times by each step (excluding the first and last step) are averaged to produce the results. The deep potential MD⁴³ simulation is performed with the LAMMPS package with one CPU core. Five repeat simulations, each lasting for 1000 steps, are conducted for each supercell size, and the time spent by each MD step is averaged. All the tests above are performed on an Intel(R) Xeon(R) Silver 4210R CPU using one core. The ab initio MD simulation is performed using the VASP package on $2 \times 2 \times 2$ and $3 \times 3 \times 3$ supercells (40 and 135 atoms, respectively) with Gamma-centered K point mesh of $3 \times 3 \times 3$ and $2 \times 2 \times 2$, respectively. For each supercell size, the simulation lasts for 100 steps. The time consumed by each step (apart from the first step) is averaged. The ab initio MD simulations are performed on the Intel(R) Xeon(R) CPU E5-2680 v3 CPU using 24 cores.

Sample deposition

The $\text{SrTiO}_3/\text{PbTiO}_3$ bilayer heterostructures are deposited by pulsed laser deposition. The PbTiO_3 films, about 40 nm in thickness, were deposited on (001)-oriented SrTiO_3 substrates with 80 nm thick SrRuO_3 electrodes, followed by depositing a 2 nm thick SrTiO_3 capping layer. The SrRuO_3 electrode, PbTiO_3 film and SrTiO_3 capping layer were deposited at 660, 620, and 700°C, respectively, using a 248-nm KrF excimer laser (COMPex Pro 205F, Coherent) with an energy flux density of 1.5 J/cm^2 on SrRuO_3 , PbTiO_3 and SrTiO_3 ceramic targets and a repetition rate of 3 Hz. 20% excessive Pb was added into the PbTiO_3 target to compensate for the Pb loss during deposition. The oxygen partial pressure for the deposition of SrRuO_3 and SrTiO_3 is 100 mTorr, and for the deposition of PbTiO_3 , is 80 mTorr.

PFM measurement

Ferroelectric domain structures of various $\text{SrTiO}_3/\text{PbTiO}_3$ bilayers were characterized at room temperature by atomic force microscope (Cypher ES, Asylum Research). NanoWorld EFM platinum/iridium-coated tips and Adama Supersharp Au tips, both 2.8 N/m in force constant, were used in PFM measurements. The ac signal applied on the tip for all the PFM measurements is 800 mV in amplitude. The samples were grounded in all the measurements. Piezoresponse phase-voltage hysteresis loops were collected in the dual a.c. resonance tracking mode. The vector PFM was conducted with different in-plane sample rotation angles to reconstruct the domain structures^{56,57}.

Data availability

The datasets generated and/or analyzed during the current study are available from the corresponding author upon reasonable request.

Code availability

The underlying code for this study is made up of the active-learning facilitated effective Hamiltonian package (ALFE-H) and is available at <https://obeyond.nju.edu.cn/Code/index.html> after registration.

Received: 5 September 2024; Accepted: 10 February 2025;

Published online: 14 March 2025

References

1. Martin, R. M. *Electronic Structure: Basic Theory and Practical Methods* (Cambridge University Press, 2004).
2. Jinnochi, R., Karsai, F. & Kresse, G. On-the-fly machine learning force field generation: Application to melting points. *Phys. Rev. B* **100**, 014105 (2019).
3. Podryabin, E. V. & Shapeev, A. V. Active learning of linearly parametrized interatomic potentials. *Comput. Mater. Sci.* **140**, 171–180 (2017).
4. Vandermause, J. et al. On-the-fly active learning of interpretable Bayesian force fields for atomistic rare events. *npj Comput. Mater.* **6**, 20 (2020).
5. Jinnochi, R., Miwa, K., Karsai, F., Kresse, G. & Asahi, R. On-the-fly active learning of interatomic potentials for large-scale atomistic simulations. *J. Phys. Chem. Lett.* **11**, 6946–6955 (2020).
6. Friederich, P., Häse, F., Proppe, J. & Aspuru-Guzik, A. Machine-learned potentials for next-generation matter simulations. *Nat. Mater.* **20**, 750–761 (2021).
7. Zhong, W., Vanderbilt, D. & Rabe, K. M. First-principles theory of ferroelectric phase transitions for perovskites: The case of BaTiO_3 . *Phys. Rev. B* **52**, 6301–6312 (1995).
8. Ghosez, P. & Junquera, J. Modeling of ferroelectric oxide perovskites: from first to second principles. *Annu. Rev. Condens. Matt. Phys.* **13**, 325–364 (2022).
9. Zhong, W., Vanderbilt, D. & Rabe, K. M. Phase transitions in BaTiO_3 from first principles. *Phys. Rev. Lett.* **73**, 1861–1864 (1994).
10. Nahas, Y. et al. Discovery of stable skyrmionic state in ferroelectric nanocomposites. *Nat. Commun.* **6**, 8542 (2015).
11. Chen, P., Paillard, C., Zhao, H. J., Íñiguez, J. & Bellaiche, L. Deterministic control of ferroelectric polarization by ultrafast laser pulses. *Nat. Commun.* **13**, 2566 (2022).
12. Chen, L., Xu, B., Yang, Y. & Bellaiche, L. Macroscopic and microscopic structures of cesium lead iodide perovskite from atomistic simulations. *Adv. Funct. Mater.* **30**, 1909496 (2020).
13. Wang, D., Bokov, A. A., Ye, Z.-G., Hlinka, J. & Bellaiche, L. Subterahertz dielectric relaxation in lead-free $\text{Ba}(\text{Zr},\text{Ti})\text{O}_3$ relaxor ferroelectrics. *Nat. Commun.* **7**, 11014 (2016).
14. Nahas, Y. et al. Microscopic origins of the large piezoelectricity of leadfree $(\text{Ba},\text{Ca})(\text{Zr},\text{Ti})\text{O}_3$. *Nat. Commun.* **8**, 15944 (2017).
15. Ma, X., Yang, Y., Bellaiche, L. & Wu, D. Large electrocaloric response via percolation of polar nanoregions. *Phys. Rev. B* **105**, 054104 (2022).
16. Choudhury, N., Walizer, L., Lisenkov, S. & Bellaiche, L. Geometric frustration in compositionally modulated ferroelectrics. *Nature* **470**, 513–517 (2011).
17. Naumov, I. I., Bellaiche, L. & Fu, H. Unusual phase transitions in ferroelectric nanodisks and nanorods. *Nature* **432**, 737–740 (2004).
18. Nahas, Y. et al. Topology and control of self-assembled domain patterns in low-dimensional ferroelectrics. *Nat. Commun.* **11**, 5779 (2020).
19. Han, L. et al. High-density switchable skyrmion-like polar nanodomains integrated on silicon. *Nature* **603**, 63–67 (2022).
20. Lu, L. et al. Topological defects with distinct dipole configurations in $\text{PbTiO}_3/\text{SrTiO}_3$ multilayer films. *Phys. Rev. Lett.* **120**, 177601 (2018).
21. King-Smith, R. D. & Vanderbilt, D. First-principles investigation of ferroelectricity in perovskite compounds. *Phys. Rev. B* **49**, 5828–5844 (1994).
22. Bellaiche, L., García, A. & Vanderbilt, D. Finite-temperature properties of $\text{PbZr}_{1-x}\text{Ti}_x\text{O}_3$ alloys from first principles. *Phys. Rev. Lett.* **84**, 5427–5430 (2000).
23. Walizer, L., Lisenkov, S. & Bellaiche, L. Finite-temperature properties of $(\text{Ba},\text{Sr})\text{TiO}_3$ systems from atomistic simulations. *Phys. Rev. B* **73**, 144105 (2006).

24. Mentzer, C., Lisenkov, S., Fthenakis, Z. G. & Ponomareva, I. Phase evolution in the ferroelectric relaxor $\text{Ba}(\text{Ti}_{1-x}\text{Zr}_x)\text{O}_3$ from atomistic simulations. *Phys. Rev. B* **99**, 064111 (2019).

25. Lou, F. et al. PASP: Property analysis and simulation package for materials. *J. Chem. Phys.* **154**, 114103 (2021).

26. Xu, C., Yu, H., Wang, J. & Xiang, H. First-principles approaches to magnetoelectric multiferroics. *Annu. Rev. Conden. Ma. P.* **15**, 85–108 (2024).

27. Dai, M., Zhang, Y., Fortunato, N., Chen, P. & Zhang, H. Active learning-based automated construction of Hamiltonian for structural phase transitions: a case study on BaTiO_3 . *J. Phys.: Condens. Matter.* **37**, 055901 (2024).

28. Mayer, F. et al. Finite-temperature investigation of homovalent and heterovalent substituted BaTiO_3 from first principles. *Phys. Rev. B* **106**, 224109 (2022).

29. Rabe, K. M. & Waghmare, U. V. Localized basis for effective lattice Hamiltonians: Lattice wannier functions. *Phys. Rev. B* **52**, 13236–13246 (1995).

30. Iñiguez, J., García, A. & Pérez-Mato, J. M. Optimized local modes for lattice-dynamical applications. *Phys. Rev. B* **61**, 3127–3130 (2000).

31. Mani, B. K., Chang, C.-M. & Ponomareva, I. Atomistic study of soft-mode dynamics in PbTiO_3 . *Phys. Rev. B* **88**, 064306 (2013).

32. Vanderbilt, D. & Zhong, W. First-principles theory of structural phase transitions for perovskites: competing instabilities. *Ferroelectrics* **206**, 181–204 (1998).

33. Escorihuela-Sayalero, C., Wojdel, J. C. & Iñiguez, J. Efficient systematic scheme to construct second-principles lattice dynamical models. *Phys. Rev. B* **95**, 094115 (2017).

34. Bartók, A. P., Payne, M. C., Kondor, R. & Csányi, G. Gaussian approximation potentials: the accuracy of quantum mechanics, without the electrons. *Phys. Rev. Lett.* **104**, 136403 (2010).

35. Zhou, Z.-H. *Machine Learning* (Springer, 2021).

36. Verdi, C., Karsai, F., Liu, P., Jinnouchi, R. & Kresse, G. Thermal transport and phase transitions of zirconia by on-the-fly machine-learned interatomic potentials. *npj Comput. Mater.* **7**, 156 (2021).

37. Nishimatsu, T., Waghmare, U. V., Kawazoe, Y. & Vanderbilt, D. Fast molecular-dynamics simulation for ferroelectric thin-film capacitors using a first-principles effective Hamiltonian. *Phys. Rev. B* **78**, 104104 (2008).

38. Wojdel, J. C. & Iñiguez, J. Ferroelectric transitions at ferroelectric domain walls found from first principles. *Phys. Rev. Lett.* **112**, 247603 (2014).

39. Uchino, K. *Piezoelectric Actuators and Ultrasonic Motors* (Kluwer Academic Publishers, Boston, 1996).

40. Noheda, B. et al. A monoclinic ferroelectric phase in the $\text{Pb}(\text{Zr}_{1-x}\text{Ti}_x)\text{O}_3$ solid solution. *Appl. Phys. Lett.* **74**, 2059–2061 (1999).

41. Das, S. et al. Observation of room-temperature polar skyrmions. *Nature* **568**, 368–372 (2019).

42. Mermin, N. D. The topological theory of defects in ordered media. *Rev. Mod. Phys.* **51**, 591–648 (1979).

43. Zhang, L., Han, J., Wang, H., Car, R. & E, W. Deep potential molecular dynamics: a scalable model with the accuracy of quantum mechanics. *Phys. Rev. Lett.* **120**, 143001 (2018).

44. Prokhorenko, S., Kalke, K., Nahas, Y. & Bellaiche, L. Large scale hybrid monte carlo simulations for structure and property prediction. *npj Comput. Mater.* **4**, 80 (2018).

45. Kornev, I. A., Bellaiche, L., Janolin, P.-E., Dkhil, B. & Suard, E. Phase diagram of $\text{Pb}(\text{Zr},\text{Ti})\text{O}_3$ solid solutions from first principles. *Phys. Rev. Lett.* **97**, 157601 (2006).

46. Akbarzadeh, A. R., Prosandeev, S., Walter, E. J., Al-Barakaty, A. & Bellaiche, L. Finite-temperature properties of $\text{Ba}(\text{Zr},\text{Ti})\text{O}_3$ relaxors from first principles. *Phys. Rev. Lett.* **108**, 257601 (2012).

47. Bellaiche, L. & Vanderbilt, D. Virtual crystal approximation revisited: application to dielectric and piezoelectric properties of perovskites. *Phys. Rev. B* **61**, 7877–7882 (2000).

48. Zhao, H. J. et al. Energetic couplings in ferroics. *Adv. Electron. Mater.* **8**, 2100639 (2022).

49. Ponomareva, I., Bellaiche, L., Ostapchuk, T., Hlinka, J. & Petzelt, J. Terahertz dielectric response of cubic BaTiO_3 . *Phys. Rev. B* **77**, 012102 (2008).

50. Blöchl, P. E. Projector augmented-wave method. *Phys. Rev. B* **50**, 17953–17979 (1994).

51. Perdew, J. P. et al. Restoring the density-gradient expansion for exchange in solids and surfaces. *Phys. Rev. Lett.* **100**, 136406 (2008).

52. Gonze, X. & Lee, C. Dynamical matrices, born effective charges, dielectric permittivity tensors, and interatomic force constants from density-functional perturbation theory. *Phys. Rev. B* **55**, 10355–10368 (1997).

53. King-Smith, R. D. & Vanderbilt, D. Theory of polarization of crystalline solids. *Phys. Rev. B* **47**, 1651–1654 (1993).

54. Metropolis, N., Rosenbluth, A. W., Rosenbluth, M. N., Teller, A. H. & Teller, E. Equation of state calculations by fast computing machines. *J. Chem. Phys.* **21**, 1087–1092 (1953).

55. Nishimatsu, T., Iwamoto, M., Kawazoe, Y. & Waghmare, U. V. First-principles accurate total energy surfaces for polar structural distortions of BaTiO_3 , PbTiO_3 , and SrTiO_3 : consequences for structural transition temperatures. *Phys. Rev. B* **82**, 134106 (2010).

56. Kim, K.-E. et al. Configurable topological textures in strain graded ferroelectric nanoplates. *Nat. Commun.* **9**, 403 (2018).

57. Kim, J., You, M., Kim, K.-E., Chu, K. & Yang, C.-H. Artificial creation and separation of a single vortex-antivortex pair in a ferroelectric flatland. *npj Quant. Mater.* **4**, 29 (2019).

Acknowledgements

We thank the useful discussions with Dr. F. Karsai in VASP Software GmbH. X.M., H.C., Z.Y., Y.Y., and D.W. thank the National Key R&D Programs of China (grant Nos. 2022YFB3807601, 2020YFA0711504), the National Natural Science Foundation of China (grant Nos. 12274201, 51725203, 51721001, 52003117 and U1932115) and the Natural Science Foundation of Jiangsu Province (grant No. BK20200262). S.P. and L.B. thanks the Office of Naval Research Grant No. N00014-21-1-2086, the Vannevar Bush Faculty Fellowship (VBFF) Grant No. N00014-20-1-2834 from the Department of Defense and the ARA Impact 3.0 Grant. J.I.G. thanks the financial support of the Luxembourg National Research Fund (FNR) through project C21/MS/15799044/FERRODYNAMICS. We are grateful to the High Performance Computing Center (HPCC) resources of Nanjing University for the calculations.

Author contributions

Y.Y. conceived and supervised this study. X.M. developed the codes for effective Hamiltonian simulation and fitting. Y.Y., X.M., and D.W. designed the examples. X.M. and Z.Y. performed simulations on the examples. H.C. and D.W. designed the experiments. H.C. prepared the sample and conducted the PFM measurement. R.H. trained the DPMD model for BaTiO_3 . S.P., Z.W., Z.Z., J.I.G., L.B., and D.W. discussed the results and provided feedback on the codes and the examples. X.M., Y.Y., and H.C. wrote the initial version of the manuscript. All authors contributed to the revision of the manuscript.

Competing interests

The authors declare no competing interests.

Additional information

Supplementary information The online version contains supplementary material available at <https://doi.org/10.1038/s41524-025-01563-z>.

Correspondence and requests for materials should be addressed to Di Wu or Yurong Yang.

Reprints and permissions information is available at
<http://www.nature.com/reprints>

Publisher's note Springer Nature remains neutral with regard to jurisdictional claims in published maps and institutional affiliations.

Open Access This article is licensed under a Creative Commons Attribution 4.0 International License, which permits use, sharing, adaptation, distribution and reproduction in any medium or format, as long as you give appropriate credit to the original author(s) and the source, provide a link to the Creative Commons licence, and indicate if changes were made. The images or other third party material in this article are included in the article's Creative Commons licence, unless indicated otherwise in a credit line to the material. If material is not included in the article's Creative Commons licence and your intended use is not permitted by statutory regulation or exceeds the permitted use, you will need to obtain permission directly from the copyright holder. To view a copy of this licence, visit <http://creativecommons.org/licenses/by/4.0/>.

© The Author(s) 2025